Theor Chem Account (2008) 120:467–478
DOI 10.1007/s00214-008-0438-3

REGULAR ARTICLE

Theoretical study of the biologically important dioxo diiron diamond core structures

Lisa M. Pérez · Charles Edwin Webster ·
Arthur A. Low · Michael B. Hall

Received: 17 October 2007 / Accepted: 29 February 2008 / Published online: 15 April 2008

Abstract Density functional theory calculations were used to investigate synthetic complexes with diiron dioxo diamond cores and models for intermediates in the catalytic cycle of methane monooxygenase (MMO). The synthetic complexes share an antiferromagnetically coupled diiron dioxo/hydroxo diamond core structure with the oxidized and reduced intermediates (H_{ox} and H_{red}, respectively) of MMO. The DFT (B3P86) calculations on model complexes of the synthetic models, with ferromagnetic coupling, reproduce the crystal structure data to within 0.05 Å and 5° for the diamond core parameters. The crystal structures of H_{ox} extracted from two different bacteria (Bath and OB3b) indicate that H_{ox} has either two bridging hydroxy ligands or one hydroxy and one water bridge. The B3P86 calculations strongly suggest that both bridging ligands in H_{ox} are hydroxy groups. The carboxylate shift established in the crystal structures of H_{red} was calculated to be a minimum at the BP86 level of theory.

Keywords Density functional theory · DFT · Methane monooxygenase · Computational

1 Introduction

Oxygen bridged dimetal complexes $M_2(\mu\text{-}X)_2$ (X=O, OH or OH_2), with a diamond core structure play an important role in a number of important enzyme and metalloprotein systems, such as methane monooxygenase (MMO, M=Fe) [1–6], ribonucleotide reductase (RNR, M=Fe) [5,7,8], photosystem II (PSII, M=Mn) [9,10], oxyhemocyanin (oxyHc, M=Cu) [11,12], and tyrosinase (Ty, M=Cu) [13]. Although synthetic manganese complexes with a $Mn_2(\mu\text{-}O)_2$ diamond core structure have been characterized with X-ray crystallography [14–18], it has only been in the past several years that iron [19–31] model complexes with a $M_2(\mu\text{-}X)_2$ diamond core structure have been prepared and characterized.

Crystal structures of the oxidized form of MMO, H_{ox}, for both *Methylococcus capsulatus* (Bath) [32–34] and *Methylosinus trichosporium* (OB3b) [35] have been determined and were found to be very similar. H_{red} has been characterized by X-ray crystallography from the Bath bacteria [32,34]. MMO has been shown to have an $Fe_2(\mu\text{-}X)_2$ (X = O, OH, or OH_2) diamond core structure at its active site for at least three of the intermediates involved in the proposed catalytic cycle shown in Scheme 1. The catalytic cycle begins with a diiron(III,III) compound (H_{ox}), which was the first form characterized by X-ray crystallography. Mössbauer results indicate that the irons in H_{ox} are high-spin Fe(III) and H_{ox} is EPR silent; therefore, H_{ox} is a diamagnetic compound with antiferromagnetically couple Fe(III) atoms. In the catalytic cycle, H_{ox} is then reduced to a ferromagnetically coupled high-spin diiron(II,II) compound (H_{red}). H_{red} then reacts with molecular oxygen to form an antiferromagnetically coupled diiron(III,III) compound (Intermediate P) [36], which is

---

Contribution to the Nino Russo Special Issue.

L. M. Pérez
Laboratory for Molecular Simulation, Texas A&M University,
3255 TAMU, College Station, TX 77843-3255, USA

C. E. Webster
Department of Chemistry, The University of Memphis,
213 Smith Chemistry Building, Memphis, TN 38152-3550, USA

A. A. Low
Department of Chemistry, Tarleton State University, Box T-0540,
Tarleton Station, Stephenville, TX 76402, USA

M. B. Hall (✉)
Department of Chemistry, Texas A&M University, 3255 TAMU,
College Station, TX 77843-3255, USA
e-mail: hall@mail.chem.tamu.edu

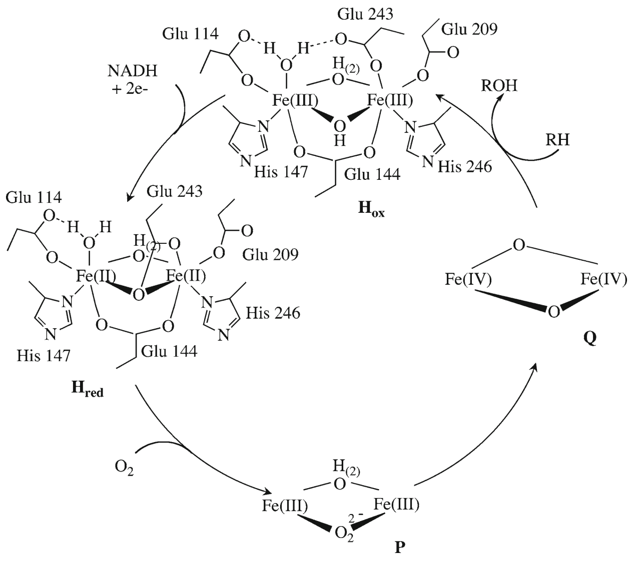

Scheme 1

proposed to be a peroxo complex. Intermediate P then rearranges to form intermediate Q, which is thought to be a high valent antiferromagnetically coupled $Fe(IV)_2O_2$ species [37]. Very little is known about the structure of Q, but extended X-ray absorption fine structure (EXAFS) [37] results indicate that Q has an asymmetric diamond core structure with the oxygen ligands bound asymmetrically between the two iron atoms. Finally, Q reacts with methane to produce the product and reform H_{ox}. The details about coordination number of the iron centers and arrangement of the ligands involved in P and Q are still ambiguous.

Que and co-workers [19–24] prepared and characterized a number of iron dimers of the general formula $Fe_2(\mu\text{-X})(\mu\text{-X}')(6\text{-Me}_3\text{-TPA})_2^{n+}$ (6-Me$_3$-TPA = tris(6-methyl-2-pyridylmethyl)amine); $X = X' = O$, $n = 2$ (**1a**(III,III)); $X = O$, X'=OH, $n = 3$ (**1b**(III,III)); $X=X'$=OH, $n = 2$ (**1c**(II,II)); and $Fe_2(\mu\text{-X})(\mu\text{-X}')(5\text{-Et}_3\text{-TPA})_2^{n+}$ (5-Et$_3$-TPA=tris(5-ethyl-2-pyridylmethyl)amine); $X=X'$=O, $n = 3$ (**1a***(III,IV)) that exhibit a diamond core structure. These compounds have structures that are closely related to the diiron diamond core structures found in the metalloenzyme methane monooxygenase [32–35,37]. In particular, the experimental model compounds $Fe_2(\mu\text{-O})_2(6\text{-Me}_3\text{-TPA})_2(ClO_4)_2$ and $Fe_2(\mu\text{-O})_2(5\text{-Et}_3\text{-TPA})_2(ClO_4)_3$, **1a**(III,III) and **1a***(III,IV), are very similar to the proposed structure for Q in MMO; their characterization with X-ray crystallography demonstrates an asymmetric diamond core structure. The distortion (degree of asymmetry) in the diamond core can be defined as the difference in the oxygen bond distance to each of the iron atoms. The difference in the two Fe–O bond lengths in the diamond core of **1a** and **1a*** is 0.08 and 0.06 Å, respectively. Distortions as large as 0.05 Å between M–O bond lengths have been observed for $Mn_2(\mu\text{-O})_2$ compounds and as little as 0.005 Å for $Cu_2(\mu\text{-O})_2$ compounds [38]. The Mössbauer data [22] and silent EPR for $Fe_2(\mu\text{-O})_2(6\text{-Me}_3\text{-TPA})_2^{2+}$ indicate antiferromagnetically coupled high-spin Fe(III) atoms. Qualitatively, each iron has five unpaired electrons, all spin up on one iron and all spin down on the other iron, creating an overall spin of zero (diamagnetic). As yet, it is unclear whether the electrons are exchange coupled directly through interaction between the iron atoms or indirectly through the bridging ligands (super-exchange). The EPR and Mössbauer data [23] for $Fe_2(\mu\text{-O})_2(5\text{-Et}_3\text{-TPA})_2^{3+}$, **1a***, indicates equivalent low-spin Fe atoms with an overall spin of 3/2. The diiron diamond core complex, $Fe_2(\mu\text{-O})(\mu\text{-OH})(6\text{-Me}_3\text{-TPA})_2^{3+}$, **1b**, has also been structurally characterized through EXAFS [39] and Mössbauer data and silent EPR indicates antiferromagnetically coupled high-spin Fe(III) atoms. Recently, the complex $Fe_2(\mu\text{-OH})_2(6\text{-Me}_3\text{-TPA})_2^{2+}$, **1c**, was synthesized and characterized through X-ray crystallography [40]; it also exhibits an asymmetric diamond core structure like that found in H_{ox}. In contrast to **1a**, and **1b**, that have antiferromagnetically coupled Fe(III) atoms, **1c** was determined to have weak ferromagnetically coupled high spin Fe(II) atoms. While the oxidation state of **1c** is the same as that found in H_{red}, the bridging ligands in the diamond core are very different (H_{red} has one bridging H_2O and a bridging oxygen from a monodentate glutamate, whereas **1c** has two bridging OH groups) and, **1c** is therefore not a good representative structure for H_{red}. The diiron diamond core complexes, **1a**, **1b**, and **1c**, represent an excellent opportunity to test DFT's ability to model weakly coupled diiron diamond core compounds and to probe the effect that protonation of the bridging oxo groups has on the Fe–Fe bond distance.

Recently, there have been a variety of theoretical investigations on dimetallic diamond-core biologically relevant systems, such as MMO, [41–55] oxyHc [56,57], Ty [58], RNR [49,59,60], and PSII [61–63]. One of the difficulties with the theoretically modeling of MMO, OxyHc, and PSII is giving a proper description for the antiferromagnetic coupling of the electrons between the metal centers. Previous theoretical work has handled the antiferromagnetic coupling by simulating the antiferromagnetic coupling with ferromagnetic coupling or the antiferromagnetic coupling was represented through a localized projection approach [41,42,48,49,64,65] A variety of theoretical models [41–53] for MMO have been implemented with the largest model studied by Dunietz et al. [41,42], which contained all first shell residues and two of the second shell residues for a total of approximately 100 atoms. The large model study indicated that it was necessary to include two of the second shell residues and two appropriate constraints to achieve the appropriate orientation of the ligands bound to the iron atoms and to properly describe the carboxylate shift in the intermediate H_{red}.

In this study, the complexes of Que and co-workers will be modeled using density functional theory and ferromagnetic coupling. These calculations will be used to calibrate

DFT's ability to model antiferromagnetically coupled diiron diamond core compounds, which are important in a number of metalloenzymes. The relationship between the iron–iron bond distance and the degree of protonation of the bridging oxo ligands will also be investigated. Lastly, two of the intermediates found in the catalytic cycle of MMO that contain a diiron diamond core structure, H_{ox} and H_{red}, will be studied at the same DFT level of theory. The models used in this study to model H_{ox} and H_{red} do not include the protein backbone or any constraints, therefore, these calculations should give an indication of the degree of influence the protein backbone has on the structure of the active site.

2 Computational details

Full geometry optimizations were performed using density functional theory (DFT) [66] with the Becke three parameter hybrid exchange functional [67–69] and the Perdew 86 correlation functional [70] (B3P86) using the Gaussian 98/03 [71] suite of programs. A Huzinaga/Dunning [72–75] valence basis set of double-ζ quality was used for the C, N, O and H atoms. A modified version of the Hay and Wadt basis set with effective core potentials (ECP) was used for the Fe atoms. Studies by Couty and Hall [76] have shown that the correct $(n+1)p$ functions are important to achieve accurate energies. Therefore, the basis set for the Fe atoms was modified from a (341/311/41) contraction to a (341/341/41) contraction. Ferromagnetic coupling was used to represent the antiferromagnetic coupling found in the experimentally prepared compounds by Que and co-workers, H_{ox} and H_{red}. Current implementations of DFT ordinarily do not represent antiferromagnetic coupling properly [64,65], because for a system with two iron atoms where each atom is d^4 or d^5 and antiferromagnetically coupled there are a number of possible wavefunctions that DFT can converge to. This problem can be resolved using ferromagnetic coupling which has been shown to give only small differences in structure and energetics for some systems when compared to the antiferromagnetically coupled case [41,42,48,49,61–63]. Calculations were performed on the computers at the Supercomputer Facility of Texas A&M University, and on an SGI Altix 450 at the Department of Chemistry, Texas A&M University.

3 Results and discussion

3.1 Model complexes

The theoretical models **2a**, **2b**, **2c**, and **2d** shown in Fig. 1, were used to represent the experimental complexes of Que and co-workers (**1a**, **1b**, and **1c**). Since we are only interested in studying the diamond core structure, we replaced the experimental ligands with simpler ligands, shown in Fig. 1 (the tertiary nitrogen of each 6-Me_3-TPA ligand was replaced with ammonia and the three pyridyl nitrogens were replaced with $HNCH_2$ groups) and fixed the bond lengths and angles of the model ligands at the experimental values of the 6-Me_3-TPA ligands. The angles were constrained to the experimental values to emulate the rigidity of the 6-Me_3-TPA ligands. All other variables were optimized in the high spin state (S = 5). To determine the effect that fixing the bond distances of the ligands attached to the Fe atoms would have on the parameters of the diamond core structure, the bond distances were allowed to relax. As expected, without the constraint of the 6-Me_3-TPA ligand, the Fe–NH_3 bond distance increased dramatically (0.66 Å), but the parameters of the diamond core varied by no more than 0.02 Å. Therefore, all results are with the bond distances and angles of the simplified 6-Me_3-TPA ligands frozen at the crystal structure values. Important bond distances and angles of the diamond core from the optimized geometry of **2a**, **2b**, **2c**, and **2d** can be found in Table 1.

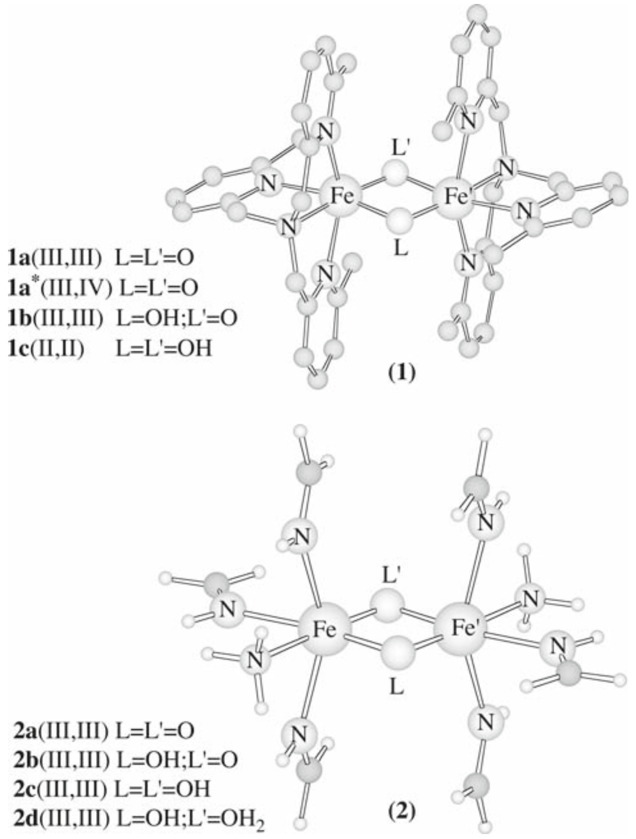

Fig. 1 (1) Experimental complexes, **1a**(III,III), **1b**(III,III), and **1c**(II,II), $Fe_2(\mu\text{-L})(\mu\text{-L}')(6\text{-}Me_3\text{-TPA})_2^{n+}$ (L=L′=O, n = 2; L=OH, L′=O, n = 3; L=L′=OH, n = 2) and **1a***(III,IV), $Fe_2(\mu\text{-L})(\mu\text{-L}')(5\text{-}Et_3\text{-TPA})_2^{n+}$ (L=L′=O, n = 3) synthesized and characterized by Que and co-workers. (2) Model compounds, **2a**(III,III), **2b**(III,III), **2c**(III,III), and **2d**(III,III), used for the B3P86 geometry optimizations

Model **2a** reproduces the Fe–Fe distance in **1a** to 0.04 Å and gives an asymmetric diamond core for the bridging oxo

Table 1 Important bond distances (Å) and angles (°) for $[\mathrm{Fe}_2^{\mathrm{III}}(\mu\text{-L})(\mu\text{-L}')]^{n+}$ shown in Fig. 1

	$[\mathrm{L}=\mathrm{L}'=\mathrm{O}]^{2+}$		$[\mathrm{L}=\mathrm{OH}, \mathrm{L}'=\mathrm{O}]^{3+}$		$[\mathrm{L}=\mathrm{L}'=\mathrm{OH}]^{4+}$		$[\mathrm{L}=\mathrm{OH}\ \mathrm{L}'=\mathrm{OH}_2]^{5+}$	
	2a	1a	2b	1b	2c	1c[a]	2d	1d
Fe–Fe	2.75	2.71	2.93	2.91	3.10	3.19	3.71	–
Fe–L	1.97	1.92	2.13	1.99	1.94	1.97	2.23	–
Fe′–L	1.84	1.84	1.95	1.99	2.09	2.17	2.00	
Fe–L′	1.84	1.84	1.83	1.82	2.09	2.17	1.94	–
Fe′–L′	1.97	1.92	1.91	1.82	1.94	1.97	2.59	
Fe–L–Fe	87.7	92.5	91.5	94.0	100.6	100.6	122.5	–
Fe–L′–Fe	87.7	92.5	101.6	106.0	100.6	100.6	108.9	–

[a] $[\mathrm{Fe}_2^{\mathrm{II}}(\mu\text{-OH})_2(6\text{-Me}_3\text{-TPA})_2]^{2+}$ X-ray crystal structure data from Ref. [40]

ligands within 0.00–0.05 Å of the experimental structure. The calculated asymmetry (0.13 Å between the short and long Fe–O bond lengths) of the diamond core is considered fairly large and may be attributed to a trans influence of the terminal ligands combined with a second order Jahn–Teller distortion. To determine if the symmetry was due entirely to a trans influence, a geometry optimization at the same level of theory was performed on the model compound $\mathrm{Fe_2O_2(NH_3)_8^{2+}}$, which would not include a trans differential influence. The optimized geometry of $\mathrm{Fe_2O_2(NH_3)_8^{2+}}$ has a symmetric diiron diamond core structure with an Fe–Fe distance of 2.75 Å and Fe–O bond distances of 1.89 Å, but the axial ammonia groups form an N–Fe–Fe–N dihedral angle of −22.9° as shown in Fig. 2. In this model it appears that the distortion of the ammonia groups to break symmetry is favored over distorting the diiron diamond core. In the experimental system, this distortion may be prevented by the constraint of the 6-$\mathrm{Me_3}$-TPA ligands; therefore, the diiron diamond core distorts instead. The differential trans influence initiates an asymmetry which allows stronger Fe–O π-bonding to one Fe that compensates for the loss of Fe–O σ-bonding to the other Fe.

The diamond core parameters of the B3P86 optimized geometry of **2b**, EXAFS, and X-ray crystal structure data for **1b**, are shown in Fig. 3. The optimized geometry of **2b** also has an asymmetric diamond core, in contrast to the results of the EXAFS for **1b**, which has both the oxo and hydroxy bridge bound symmetrically with Fe–O bond distances of 1.82 and 1.99 Å, respectively. The X-ray crystal structure for **1b** found an asymmetric diamond core structure with C_{2h} symmetry, but had disorder that could not be resolved. The disorder was thought to be caused by having two unique molecules in one unit cell where each molecule had an inversion center at the center of the diamond core and the inversion symmetry in the unit cell. The Fe–O bond distances (1.91 and 1.98 Å) found in the crystal structure were thought to be an average of the Fe–O and Fe–OH bond distances. The average value for short Fe–O and Fe–OH and long Fe–O and Fe–OH bond distances of the B3P86 optimized structure of **2b** are 1.89 and 2.02 Å, respectively, which is only 0.02 Å longer than the short Fe–O bond distance, and 0.04 Å longer than the long Fe–O bond distance in the crystal structure value. The average bond distance of the bridging oxo and hydroxide ligand with each iron in **2b** is 1.87 and 2.04 Å, respectively, which is only 0.05 Å longer than the EXAFS values of 1.82 and 1.99 Å. These results are a good indication that the asymmetry obtained in the optimized geometry is not an artifact of the level of theory or other approximations used. Compound **2b** has an asymmetry of 0.17 Å for the OH bridging ligand and 0.08 Å for the O bridging ligand. The calculated Fe–Fe distance (2.93 Å) of **2b** is within 0.02 Å of the EXAFS (2.91 Å) and X-ray crystal structure values (2.94 and 2.95 Å) and is 0.18 Å longer than the Fe–Fe bond distance calculated for **2a** (2.75 Å).

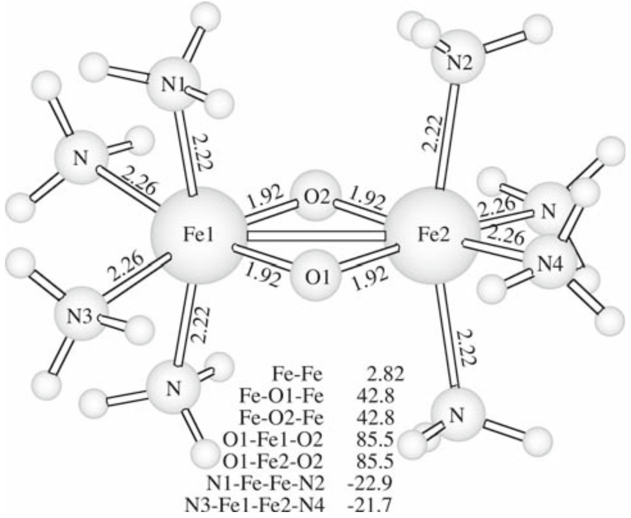

Fig. 2 B3P86 optimized structure of $\mathrm{Fe_2O_2(NH_3)_8^{2+}}$

The optimized geometry of **2c** also has a significant asymmetry in the diamond core structure with a difference of 0.15 Å for the Fe–OH bond distances and an Fe–Fe bond

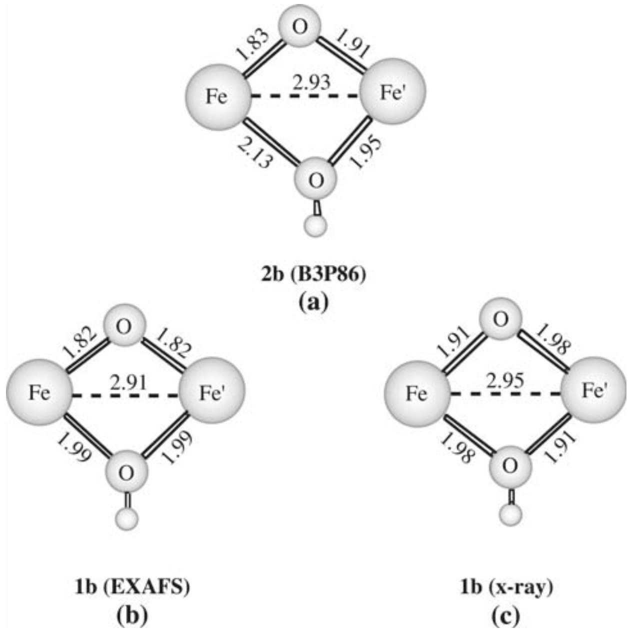

Fig. 3 Diamond core parameters for the: **a** B3P86 optimized structure of **2b**, **b** EXAFS analysis of the synthetic complex **1b**, and **c** X-ray crystal structure data that has unresolved disorder for the synthetic complex **1b**

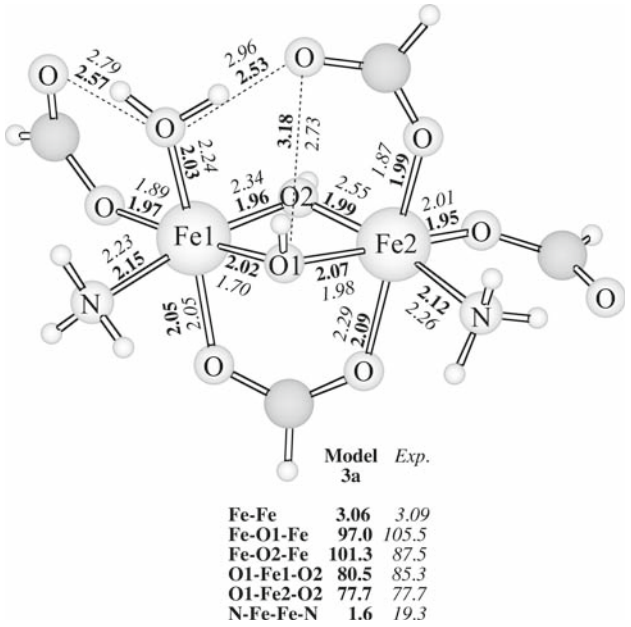

Fig. 4 The B3P86 optimized geometry of $Fe_2(\mu\text{-}OH)_2$ (**3a**) model for H_{ox}

distance of 3.10 Å, which is 0.17 Å longer than the Fe–Fe bond distance in **2b** (2.93 Å). The X-ray crystal structure of **1c** has an Fe–Fe distance of 3.19 Å and asymmetry of 0.20 Å, but the Mössbauer for **1c** indicates that the iron atoms are in the +2 oxidation state, while **2c** was calculated with the iron atoms in the +3 oxidation state. It might appear that the change in the oxidation state of the iron atoms (II or III) has very little effect on the Fe–Fe bond distance and the asymmetry of the diamond core. However, when this structure was optimized with the iron atoms in the +2 oxidation state the bridging hydroxide groups became almost symmetrically bound to the iron atoms (Fe–L = 2.04 Å and Fe′–L = 2.07 Å) but the Fe–Fe distance remained at 3.19 Å. In this structure the Fe–Fe bond distances appear to be in good agreement, but the presence or absence of the asymmetry is sensitive to small differences in ligand environment and methodology.

Lastly, a fourth theoretical model with one hydroxide and one water bridge, **2d**, was investigated to observe the Fe–Fe bond-lengthening trend with protonation of both bridging oxo groups. This model is purely theoretical since an experimental counterpart has not been characterized. Once again, **2d** has an optimized geometry with a asymmetric diamond core structure. The hydroxide bridge has an asymmetry of 0.23 Å and the water bridge has become almost terminal with Fe–OH_2 bond distances of 1.94 and 2.59 Å. The Fe–Fe bond distance was calculated to be 3.71 Å, a value significantly longer than the other models studied. The reason for the dramatic increase in the Fe–Fe bond distance of **2d** is due to the loss of a second bridging ligand that holds the iron atoms closer together. A similar compound, $Fe_2O(TPA)_2(H_2O)^{4+}$ (TPA = tris(2-pyridylmethyl)amine) was characterized by X-ray crystallography [24] and has an Fe–Fe distance of 3.57 Å, so our results appear to be reasonable.

Overall, the Fe–Fe distance increases 0.18 Å from **2a** → **2b**, 0.17 Å from **2b** → **2c**, and 0.61 Å from **2c** → **2d**. This lengthening effect with protonation has also been shown to occur in the series of manganese complexes $[Mn_2(\mu\text{-}O)_2(salpn)_2]$ (Mn–Mn = 2.7 Å, salpn=N,N'-propylenebis(salicylidenimine)), $[Mn_2(\mu\text{-}O)(\mu\text{-}OH)(salpn)_2]^+$ (Mn–Mn = 2.8 Å), $[Mn_2(\mu\text{-}OH)_2(salpn)_2]^{2+}$ (Mn–Mn = 2.9 Å), where a lengthening of 0.1 Å was observed in the Mn–Mn distance with each protonation of the oxo bridge [77]. It is interesting to note that the Fe–Fe bond distance increases twice as fast as the Mn–Mn bond distance upon protonation of the bridging oxo ligands.

4 Methane monooxygenase models

4.1 Oxidized form (H_{ox})

For this system, H_{ox} was modeled by replacing the histidines in the first coordination sphere with ammonias and the glutamates in the first coordination sphere with formate ligands (Fig. 4). The models were then fully optimized at the B3P86 level with $S = 5$ and compared with the available X-ray crystal structure data. In all available crystal structures for H_{ox}, the first bridging ligand (on the side with the histidine ligands)

Table 2 X-ray crystal structures determined for H_{ox}

	Bath	Bath	Bath	Bath	OB3b	OB3b
Resolution (Å)	2.2[a]	1.7[b]	1.96[c]	1.96[c]	2.0[d]	2.7[d]
Temp. (°C)	4	−160	−175	−175	18	18
Comp. B present	NO	NO	NO	NO	NO	YES[e]
Second bridging ligand	Acetate	H_2O	Formate	OH	OH	OH
Fe–Fe (Å)	3.41	3.09[f]	3.2	3.2	2.99	3.07

[a] Ref. [78]

[b] Ref. [34]

[c] Ref. [32]

[d] Ref. [35]

[e] Crystals were grown in a solution containing MMOB in a molar ration 2MMOB:1 MMOH, but component B was not found in the resulting crystals

[f] Average value for the Fe–Fe bond distance in protomer A and protomer B

was assigned as an hydroxide, but there was some question as to whether the second bridging diamond core ligand in H_{ox} was a water or hydroxide. Six different crystal structures of H_{ox} have been determined (Table 2) and all are very similar with the following four exceptions: (1) the hydroxylase component (MMOH) of soluble MMO from OB3b crystallized (Fig. 5a) as a monomer per asymmetric unit with a two-fold axis, whereas MMOH from Bath crystallized (Fig. 5b) as a dimer per asymmetric unit; (2) the original crystal structure for MMOH from Bath [78] (Fig. 5f, g) had an exogenous acetate as the second bridging ligand in the diamond core for both protomer A and B; (3) a crystal structure for MMOH from Bath [32] had an exogenous formate for the second bridging ligand in protomer A; and (4) the identity of the second bridging ligand in the diamond core (hydroxide or water). The acetate ligand found in the earliest crystal structure for H_{ox} is believed to come from the buffer solution and illustrates that the active site is somewhat flexible.

To investigate the possible identity of the second bridging ligand (OH or H_2O) in both the Bath and OB3b crystal structures, two theoretical models (**3a** and **3b**) were optimized in the $Fe(III)_2$ high spin state ($S = 5$). Compound **3a** has two hydroxide bridges, where **3b** has an hydroxide bridge and a water bridge on the side with the glutamate ligands. The optimized geometry of **3a** is shown in Fig. 4 and the pertinent bond distances for **3a** and **3b** are given in Table 3. There is an estimated standard deviation of 0.2 for the 1.7 Å Bath structure, 0.29 Å for the 1.96 Å Bath structure, and 0.15 Å for the OB3b structure bond distances according to a Luzzati plot, but these estimates are often high. The Fe–Fe bond distance of **3a** (3.06 Å) is within the experimental uncertainty of the crystal structure values[1] (3.04, 3.14, 3.18, 3.16, and 2.99 Å). The Fe–Fe distance for **3b** (3.48 Å) is 0.30–0.48 Å longer than the crystal structure results. It should also be noted that the “bridging” water in **3b** migrated to one of the irons and became a terminal ligand with Fe–O distances of 2.05 and 3.37 Å. The water molecule might be hydrogen bonded to the protein backbone, which could keep it in the bridging position, therefore, a second calculation was performed (**3b**′) where the Fe–O bond distances for the bridging water ligand in **3b** were fixed to the Bath 1.7 Å crystal structure values (average between protomer A and B, 2.34, 2.55 Å). The resulting optimized structure had an Fe–Fe distance of 3.30 Å, which is still 0.16 Å longer than the crystal structure value (3.09 Å). Our results for the calculated Fe–Fe distance in the Que models also indicate that the Fe–Fe distance would be too long with a bridging water molecule unless the protein backbone is holding the iron atoms together. Since a crystal structure of H_{ox} was determined with an exogenous acetate group as the second bridging ligand, and an Fe–Fe distance of 3.46 Å (Protomer A) and 3.36 Å (Protomer B) indicates that the active site is fairly flexible and that the protein backbone is not holding the Fe atoms together in H_{ox}. The good agreement of the Fe–Fe distance between the crystal structure of H_{ox} and **3a** along with the poor agreement in **3b** and **3b**′, provides a strong argument that H_{ox} has a core structure of $Fe_2(OH)_2$ and not $Fe_2(OH)(OH_2)$.

Compound **3a** has an Fe–Fe distance of 3.06 Å which is only 0.03 Å shorter than the Bath structure (3.09) and 0.07 Å longer than the OB3b structure (2.99 Å), an error well within the accuracy of the crystal structure. There are three main discrepancies between the optimized geometry of **3a** and the crystal structures of H_{ox}. The first difference is that the first bridging ligand (μ-OH) in all of the crystal structures are asymmetrically bound to the iron atoms, whereas in all theoretical models, the first hydroxide bridge is bound nearly symmetric. In the crystal structures there is an interaction between the bridging hydroxide hydrogen and the oxygen

---

[1] Photoreduction of the active site can occur during the protein structure determination thereby effecting the Fe–Fe distance and other structural parameters.

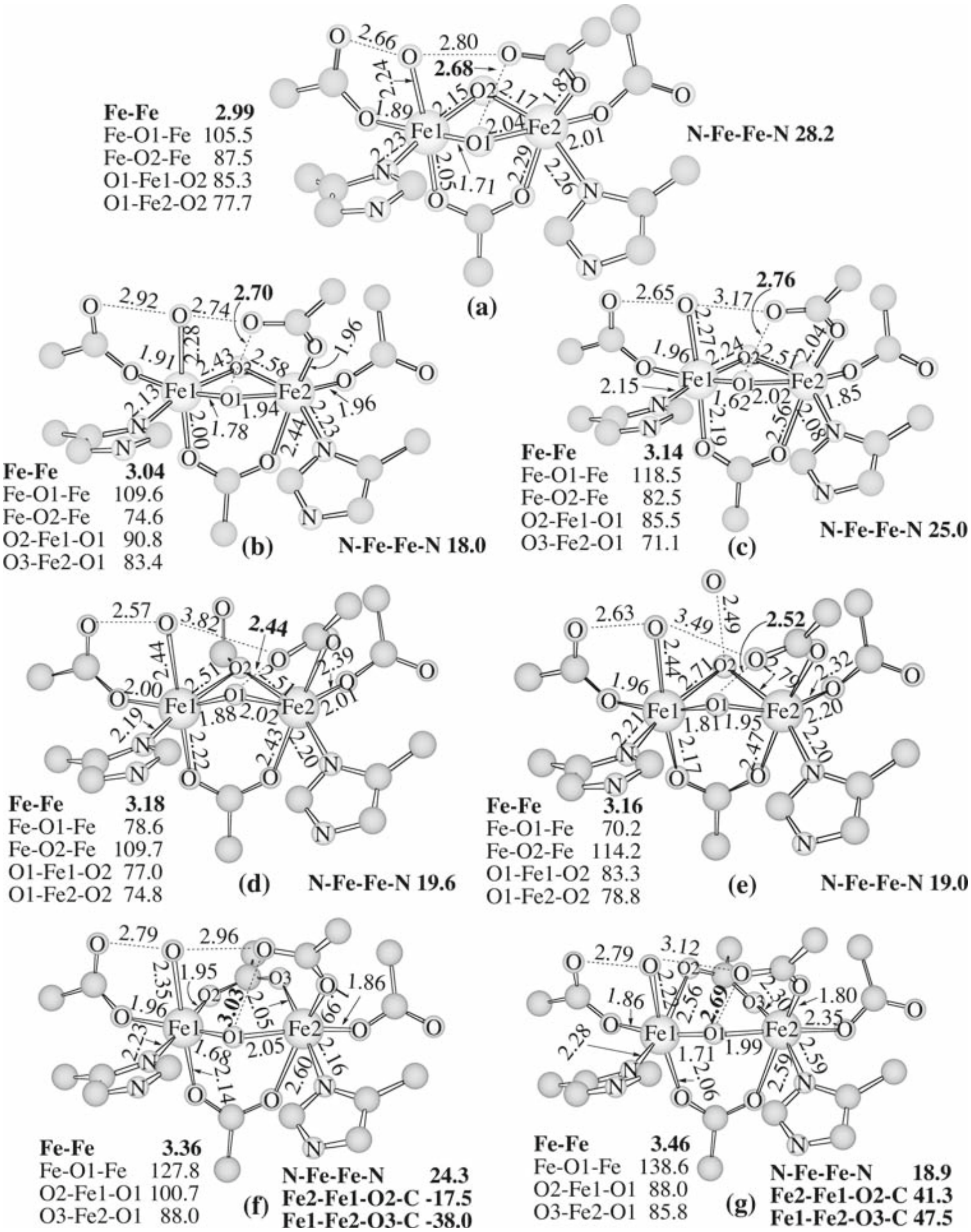

Fig. 5 **a** 2.0 Å resolution X-ray crystal structure of H_{ox} from OB3b. **b** 1.7 Å resolution X-ray crystal structure of H_{ox} from Bath, protomer A. **c** 1.7 Å resolution X-ray crystal structure of H_{ox} from Bath, protomer B. **d** 1.96 Å resolution X-ray crystal structure of H_{ox} from Bath, protomer A. **e** 1.96 Å resolution X-ray crystal structure of H_{ox} from Bath, protomer B. **f** 2.2 Å resolution X-ray crystal structure of H_{ox} with an exogenous acetate group from Bath, protomer A. **g** 2.2 Å resolution X-ray crystal structure of H_{ox} with an exogenous acetate group from Bath, protomer A

group of the Glu243 (Fig. 5) with O···O distances from 2.44 to 3.03 Å. In the theoretical models, there is an interaction between the hydroxide hydrogen and the oxygen group of the acetate representing Glu243 (Figs. 4, 6, and 7) with O···O bond distances from 2.63–3.18 Å. It is plausible that the location of Glu243 could effect the Fe–O bond distances of the bridging hydroxide ligand, but a direct correlation between the location of Glu243 and the OH ligand did not present itself. Therefore, the origin of the asymmetric binding in the crystal structures for the bridging hydroxide group, which lies on the same side as the histidine ligands, is unclear. In the Dunietz et al. work, the histidine ligands were included (capped at the C_α with a hydrogen) in the theoretical model, but their results also showed a symmetrically bound hydroxide ligand. This result indicates that the histidine groups are not responsible for the asymmetric binding of the hydroxide ligand. Also, their work employed the 6-31G(d) basis set on all heteroatoms attached to the iron atoms, therefore, it appears that it is not the basis set causing this difference. The second difference between the optimized structure **3a**, and the crystal structures for H_{ox}, is the orientation of formate ligand representing Glu209. In the crystal structures, Glu209 is oriented such that it is perpendicular to the Fe–O1–Fe plane, whereas in all models, the formate representing Glu209 rotates to lie in the Fe–O1–Fe plane, and hydrogen bonds with the ammonia ligand or the second bridging ligand. Dunietz et al. concluded that the H-bonding network is important to achieve the proper orientation of Glu209 ligand, but our results suggest that the orientation of the Glu209 ligand does not appear to be important to reproduce

Table 3 Important bond distances (Å) for H_{ox} crystal structures[a] and optimized structures (**3a**, **3b**, **3c**, and **3d**)

	Fe–Fe	Fe1–O1	Fe2–O1	Fe1–O2	Fe2–O2
Bath					
Protomer A[a] (μ-OH_2)	3.04	1.78	1.94	2.43	2.58
Protomer B[a] (μ-OH_2)	3.14	1.62	2.02	2.24	2.51
Avg.	3.09	1.70	1.98	2.34	2.55
Protomer A[b] (μ-O(CHO))	3.18	1.88	2.02	2.51	2.51
Protomer B[b] (μ-OH)	3.16	1.81	1.95	2.71	2.79
OB3b[c] (μ-OH)	2.99	1.71	2.04	2.15	2.17
Fe_2(μ-OH)$_2$ **3a**	3.06	2.02	2.07	1.96	1.99
Fe_2(μ-OH)(μ-OH_2) **3b**	3.48	1.97	1.93	2.05	3.37
Fe_2(μ-OH)(μ-O(CHO)) **3d**	3.12	2.03	2.05	2.04	2.05
	Fe–Fe	Fe1–O1	Fe2–O1	Fe1–O2	Fe2–O3
Bath					
Protomer A[d] (μ-OAc)	3.36	1.68	2.05	1.95	2.05
Protomer B[d] (μ-OAc)	3.46	1.71	1.98	2.56	2.30
Avg.	3.41	1.70	2.02	2.25	2.18
Fe_2(μ-OH)(OAc) **3c**	3.53	1.96	2.05	2.02	2.05

[a] Values in parenthesis for each crystal structure indicate the assigned identity of the second bridging ligand. In all crystal structures of H_{ox}, the first bridging ligand is assigned as an hydroxy group

[b] X-ray crystal structure data for 1.7 Å resolution at −160 °C (Ref. [34])

[c] X-ray crystal structure data for 1.96 Å resolution at −175 °C (Ref. [32])

[d] X-ray crystal structure data for 2.0 Å resolution at 18 °C (Ref. [35])

[e] X-ray crystal structure data for 2.2 Å resolution at 4 °C w/ acetate ligand (Ref. [78])

the Fe–Fe bond distance or the diamond core structure. The third difference, involves the orientation of the two ammonia groups in the model compounds that are used to describe the histidine ligands. In the crystal structures of H_{ox} the histidine ligands are "twisted" relative to one another. The N–Fe–Fe–N dihedral angle is a good measurement for the magnitude of "twisting" for the ammonia/histidine ligands. The "twist" dihedral for the H_{ox} crystal structures ranges from 18.0 to 28.2° whereas in the computed models, the "twist" dihedral angles are less than 2°. Apart from these three small differences, our model compound, **3a**, is in good agreement with the crystal structure of H_{ox} for the Fe–Fe distance and in qualitative agreement for the ligands even though it contains only the local Fe environment.

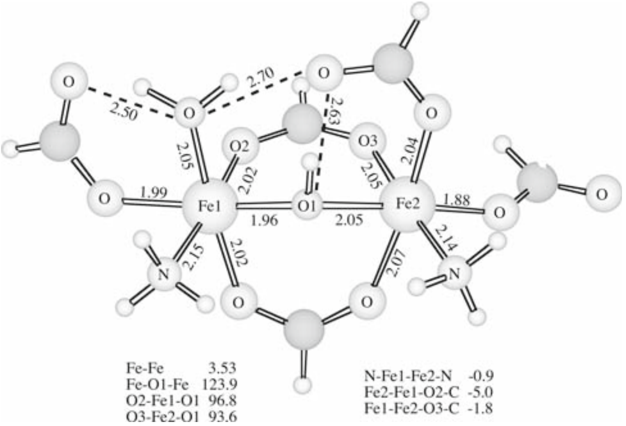

Fig. 6 The B3P86 optimized geometry of Fe_2(μ-OH)(OAc) (**3c**) model for H_{ox}

As another test of DFT's ability to accurately reproduce the compounds of MMO, two other models were studied, where the second bridging ligand was replaced with a formate group, **3c** and **3d**, and compared with the X-ray crystal structure of H_{ox} with an exogenous acetate (Fig. 5f, g) or formate ligand (Fig. 5d). The optimized structure of **3c** can be found in Fig. 6, and important geometrical parameters in Table 3. The Fe–Fe distance in the optimized structure of **3c** (3.53 Å) is 0.17 Å longer than the Fe–Fe distance in protomer A (3.36 Å) and 0.07 Å longer than the Fe–Fe distance found in the protomer B (3.46 Å). The overestimation of the Fe–Fe bond distance in **3c** is thought to be caused by the difference in the "twist" of the formate ligand of the model compound, **3c**. As a measure of the "twist" of the exogenous formate/acetate group, we can compare the "twist" dihedral angles Fe2–Fe1–O2–C and Fe1–Fe2–O3–C. In the X-ray crystal structure of Bath protomer A (Fig. 5f, g), the "twist" dihedral angles are −17.5° and −38.0°, (Fe2–Fe1–O2–C and Fe1–Fe2–O3–C, respectively) and in Bath protomer B, 41.3° and 47.5°. In **3c**

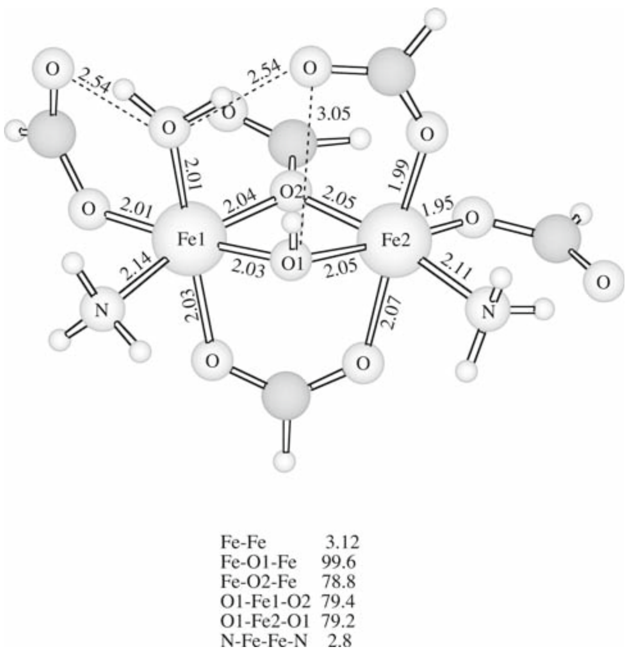

Fig. 7 The B3P86 optimized structure of $Fe_2(\mu\text{-OH})(\mu\text{-O(CHO)})$ (**3d**) for H_{ox}

the "twist" dihedral angles are −5.0° and −1.8°. The limited flexiblity of the active site could be restricting the Fe–Fe distance to approximately 3.5 Å, which could cause the acetate ligand to twist to remain bridged to both iron atoms, but an X-ray crystal structure of MMOH that was soaked in DMSO showed an Fe–Fe distance of 3.7 Å [79]. In this case, it is possible that the twist of the acetate ligand is due to the orientation of the histidine ligands, which have N–Fe–Fe–N dihedrals of 24.3° and 18.9° in the crystal structure (protomers A and B, respectively). For the oxygen atoms in the acetate ligand to remain trans to the nitrogen atoms of the histidine ligands, they would have to "twist", which may cause the Fe–Fe distance to be shorter. Therefore, the orientation of the ammonia ligands, that represent the histidine ligands, may be essential to reproduce the Fe–Fe distance found in this crystal structure. While the orientation of the representative histidine ligands in **3a** did not effect its Fe–Fe distance, the orientation of the histidine ligands may have an effect on the Fe–Fe distance of other species that contain a second bridging ligand that prefers a position trans to the histidine ligands. The optimized structure of **3d** can be found in Fig. 7, and important geometrical parameters in Table 3. The Fe–Fe distance in the optimized structure of **3d** (3.12 Å) is 0.06 Å shorter than the Fe–Fe distance in protomer A (3.12 Å) and 0.04 Å shorter than the Fe–Fe distance found in the protomer B (3.16 Å), in excellent agreement with the crystal structure data. As with **3a** and **3b**, the Fe–O bond distances for the first bridging ligand (μ-OH) are essentially symmetric (2.03 and 2.05 Å), whereas, they are asymmetric in the crystal structure (1.88 and 2.02 Å, protomer A; 1.81 and 1.95 Å, protomer B), but are still within reasonable error bounds. In **3d**, the exogenous formate ligand rotates from the crystal structure orientation (Fig. 5d) to allow the hydrogen to interact with the O of Glu209. In the crystal structure, the terminal oxygen of the exogenous formate is hydrogen bonded to a water molecule.

Overall, these results indicate that the second bridging ligand in H_{ox} (without exogenous ligands from the buffer solution) is a hydroxide and not a water ligand. These results also show that the protein backbone does not have a significant effect on the Fe–Fe distance in H_{ox}, where both bridging ligands are of the form (μ-OX, X=H, or CHO), but may have an effect on the Fe–Fe distance when an exogenous acetate group replaces the second hydroxide group. The theoretical model used in this study (**3a**) with ferromagnetic coupling at the B3P86 level of theory was found to give reasonable results for the antiferromagnetically coupled intermediate H_{ox}.

4.2 Reduced form (H_{red})

The intermediate H_{red} differs from H_{ox} in that the first bridging ligand (μ-OH) of H_{ox} is displaced by the β-oxygen atom in Glu243 due to a carboxylate shift of Glu243 from a terminal to a bidentate and bridging ligand (Fig. 8). The theoretical models for H_{red}, **4a** and **4a**′, have the histidines replaced with ammonias, the glutamates with formates, and a water as the first bridging ligand. The B3P86 optimized structure, **4a**′, is shown in Fig. 9a. Upon optimization, the bidentate carboxylate returns to a bridging conformation, the bridging water becomes terminal, one of the iron atoms becomes 5 coordinate, and the Fe–Fe distance increases to 3.87 Å, as opposed to the X-ray crystal structure Fe–Fe distance of 3.28 Å. A variety of starting structures and orbital occupations were investigated and in all cases, the carboxylate shift was lost. To ascertain how a carboxylate shift would change the Fe–Fe bond distance, the bridging oxygen of the carboxylate shift ligand was fixed at Fe–O bond distances of 2.2 Å along with the axial $Fe\text{–}OH_2$ bond distance[2] and the rest of the structure was optimized. The Fe–Fe bond distance did decrease slightly (3.78 Å) but is still far too long. Dunietz et al. also lost the carboxylate shift for their small model, which only included the C-α capped first shell residues at the B3LYP level of theory. The large model used by Dunietz et al. added the second shell residues Asp143 and Asp242, which are attached to Glu144 and Glu243. The β carbons of the Asp143 and Asp242 were constrained to simulate the effect of the four-helix bundle in the protein, and the terminal oxygen to iron bond distance of Glu209 was constrained

---

[2] The Fe–O bond distance of the terminal water ligand was frozen, because it was found that during the geometry optimization large geometry steps were taken that involved this bond distance changing by 0.1–0.2 Å in one step.

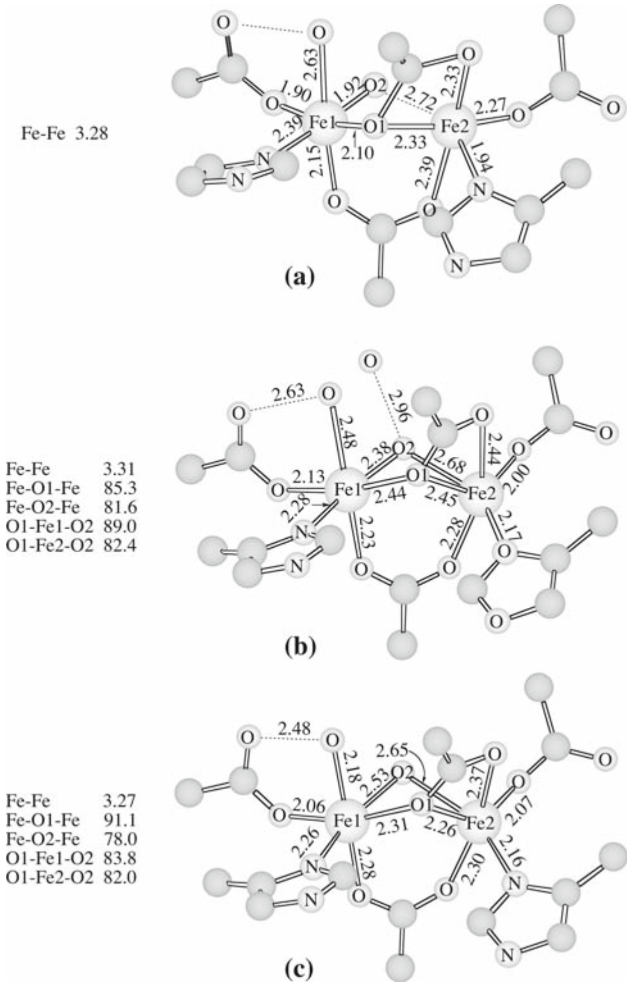

Fig. 8 **a** 1.7 Å resolution X-ray crystal structure of Bath active site for H_{red} from protomer A. Protomer B was thought to be only partially reduced to an Fe(II)–Fe(III) state and was found to closely resemble the geometry found in H_{ox}. **b** 2.15 Å resolution X-ray crystal structure of Bath active site for H_{red}, protomer A and **c** protomer B

to the crystal structure value to simulate a hydrogen bonding interaction between Glu209 and a previously unresolved water molecule. With the large model and the aforementioned constraints, they were able to obtain a carboxylate shift, and an Fe–Fe distance of 3.5 Å. These authors concluded that the hydrogen bonding network stablilized the carboxylate shift. To investigate possible deficencies in the method and/or basis set used, model **4a** was fully optimized at the Becke Perdew 86 (BP86) [67,70] level of theory, with a double-ζ quality basis set plus polarization [80] (6-31G(d')) on C, O, and N, a double-ζ quality basis set [81] (6-31G) for H, and the modified double-ζ basis set plus ECP as described in the theoretical methods section for Fe. The fully optimized geometry of **4a** at the BP86 level of theory is shown in Fig. 9b, and a carboxylate shift was maintained. The optimized Fe–Fe bond distance in **4a** is 3.50 Å, which is 0.19–0.23 Å longer than the crystal structure data, but is within the Luzzati coordinate error of 0.24 Å. Based on these results, it appears that the protein backbone and the hydrogen bonding network are not necessary to obtain a carboxylate shift.

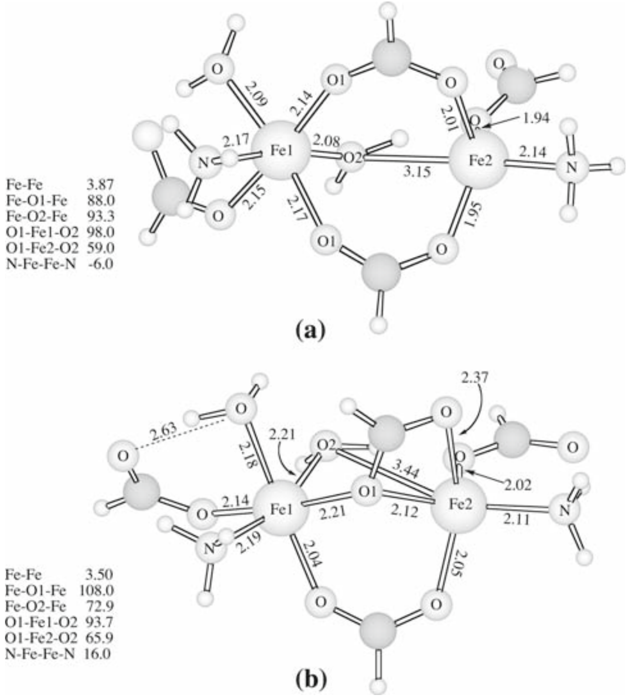

Fig. 9 **a** B3P86 optimized structure of **4a**′ and **b** BP86 optimized structure of **4a** for H_{red}

5 Conclusions

Density functional theory calculations on the theoretical models **2a**, **2b**, **2c**, and **2d** were compared to experimental complexes of Que and co-workers (**1a**, **1b**, and **1c**) and showed that B3P86 calculations are capable of reproducing the core parameters in antiferromagnetically coupled diiron diamond core compounds. Models **2a**, **2b**, and **2c** reproduced the Fe–Fe distance in **1a**, **1b**, and **1c** to within 0.02, 0.04, and 0.09 Å, respectively. All models optimized with an asymmetric diamond core that may be attributed to a trans influence of the terminal ligands combined with a second order Jahn–Teller distortion. In the protonation series, the Fe–Fe distance increases 0.18 Å from **2a** → **2b**, 0.17 Å from **2b** → **2c**, and 0.61 Å from **2c** → **2d**, where the dramatic increase in the Fe–Fe distance from **2c** → **2d** is due to the water ligand moving from a bridging to a terminal position.

Based on the excellent agreement of the Fe–Fe distance for **3a** and the poor agreement for **3b** with the crystal structure, the second bridging ligand in H_{ox} (without exogenous ligands from the buffer solution) is a hydroxide and not a water ligand. The results also indicate that the protein backbone does not have a significant effect on the Fe–Fe bond distance in H_{ox}, when both bridging ligands are of the form (μ-OX, X=H, or CHO), but may have an effect on the Fe–Fe distance when an exogenous acetate group replaces the second bridging group.

The BP86 optimized structure of **4a** represents the first simple theoretical model for H_{red} that maintains a carboxylate shift, has an Fe–Fe distance within the error of the crystal structure, contains all first shell residues, is fully optimized, and without any second shell residues or water molecules. Thus, it may constitute one of the simplest models for use in studying the remaining steps in the catalytic cycle of methane monooxygenase.

Acknowledgments We thank The Welch Foundation (A-0648) and the National Science Foundation (CHE-0518074 and CHE-0541587) for their generous support. We would also like to thank the Supercomputing Facility at Texas A&M University for computer time.

References

1. Merkx M, Kopp DA, Sazinsky MH, Blazyk JL, Müller J, Lippard SJ (2001) Angew Chem Int Ed 40:2782
2. Du Bois J, Mizoguchi TJ, Lippard SJ (2000) Coord Chem Rev 200:443
3. Lipscomb JD, Que L Jr (1998) JBIC 3:331–336
4. Wallar BJ, Lipscomb JD (1996) Chem Rev 96:2625
5. Solomon EI, Brunold TC, Davis MI, Davis MI, Kemsley JN, Lee S, Lehnert N, Neese F, Skulan AJ, Yang Y, Zhou J (2000) Chem Rev 100:235
6. Kovaleva EG, Neibergall MB, Chakrabary S, Lipscomb JD (2007) Acc Chem Res 40:475–483
7. Nordlund P, Eklund H (1995) Curr Opin Struct Biol 5:758
8. Riggs-Gelasco PJ, Shu L, Shuxian C, Burdi D, Huynh BH, Que L Jr, Stubbe J (1998) J Am Chem Soc 120:849–860
9. Yachandra VK, Sauer K, Klein MP (1996) Chem Rev 96:2927
10. Yachandra VK, DeRose VJ, Latimer MJ, Mukerji I, Sauer K, Klein MP (1993) Science 260:675
11. Magnus KA, Hazes B, Ton-That H, Bonaventura C, Bonaventura J, Hox WGJ (1994) Proteins: Struct, Funct, Genet 19:302–309
12. Magnus KA, Ton-That H, Carpenter JE (1994) Chem Rev 94:727–735
13. Solomon EI, Sundaram UM, Machonkin RE (1996) Chem Rev 96:2563
14. Baldwin MJ, Stemmler TL, Riggs-Gelasco PJ, Kirk ML, Penner-Hahn JE, Pecoraro VL (1994) J Am Chem Soc 116:11349
15. Glerup J, Goodson PA, Hazell A, Hazell R, Hodgson DJ, McKenzie CJ, Michelsen K, Rychlewska U, Toftlund H (1994) Inorg Chem 33:4105
16. Kitajima N, Singh UP, Amagai H, Osawa M, Moro-oka Y (1991) J Am Chem Soc 112:7757
17. Goodson PA, Oki AR, Glerup J, Hodgson DJ (1990) J Am Chem Soc 112:6248
18. Stebler M, Ludi A, Bürgi HB (1986) Inorg Chem 25:4743
19. MacMurdo VL, Zheng H, Que L Jr (2000) Inorg Chem 39:2254
20. Petasis D, Hsu H, Dong Y, Shu L, Young VG Jr, Que L Jr (1999) J Am Chem Soc 121:5230
21. Zheng H, Zang D, Young VG Jr, Que L Jr (1999) J Am Chem Soc 121:2226
22. Zang Y, Dong Y, Que L Jr, Kauffmann K, Münck E (1995) J Am Chem Soc 117:1169
23. Dong Y, Fujii H, Hendrick MP, Leising RA, Pan G, Randall CR, Wilkinson EC, Zang Y, Que L Jr, Fox BG, Kauffmann K, Münck E (1995) J Am Chem Soc 117:2778
24. Zang Y, Pan, Gaofeng P, Que L Jr, Fox BG, Münck E (1994) J Am Chem Soc 116:3653
25. Lee D, Lippard SJ (2001) J Am Chem Soc 19:4611
26. He C, Lippard SJ (2001) J Inorg Chem 47:1414
27. Barrios AM, Lippard SJ (2001) Inorg Chem 40:1060
28. He C, Lippard SJ (2000) J Am Chem Soc 122:184
29. Lee D, Du Bois J, Petasis D, Hendrich MP, Krebs C, Hanh Huynh B, Lippard SJ (1999) J Am Chem Soc 42:9893
30. Mizoguchi TJ, Davydov RM, Lippard SJ (1999) J Inorg Chem 38:4098
31. Lee D, Lippard SJ (1998) J Am Chem Soc 120:12153
32. Whittington DA, Lippard SJ (2001) J Am Chem Soc 123:827
33. Rosenzweig AC, Brandstetter H, Whittington DA, Nordlund P, Lippard SJ, Frederick CA (1997) Proteins 29:141
34. Rosenzweig AC, Nordlund P, Takahara PM, Fredrick CA, Lippard SJ (1995) Chem Biol 2:409
35. Elango N, Radhakrishnan R, Froland WA, Wallar BJ, Earhart CA, Lipscomb JD, Ohlendorf DH (1997) Protein Sci 6:556
36. Lui KE, Valentine AM, Qui D, Edmondson DE, Appelman EH, Spiro TG, Lippard SJ (1995) J Am Chem Soc 117:4997
37. Shu L, Neshein JC, Kauffmann K, Münck E, Lipscomb JD, Que L (1997) Science 275:515
38. Wilkinson EC, Dong Y, Zang Y, Fujii H, Fraczkeiwicz R, Fraczkiewicz G, Czernuszewicz RS, Que L Jr (1998) J Am Chem Soc 120:955–962
39. Zang Y, Pan G, Que L Jr (1994) J Am Chem Soc 116:3653–3654
40. MacMurdo VL, Zheng H, Que L Jr (2000) Inorg Chem 39:2254
41. Gherman BF, Dunietz BD, Whittington DA, Lippard SJ, Friesner RA (2001) J Am Chem Soc 123:3836
42. Dunietz BD, Beachy MD, Cao Y, Whittington DA, Lippard SJ, Friesner RA (2000) J Am Chem Soc 122:2828
43. Torrent M, Mogi K, Basch H, Musaev DG, Morokuma K (2001) J Phys Chem B 105:8616
44. Basch H, Musaev DG, Morokuma K (2001) J Phys Chem B 105:8452
45. Torrent M, Musaev DG, Morokuma K (2001) J Phys Chem B 105:4453
46. Torrent M, Musaev DG, Morokuma K (2001) J Phys Chem B 105:322
47. Basch H, Mogi K, Musaev DG, Morokuma K (1999) J Am Chem Soc 121:7249
48. Siegbahn PEM (2001) J Biol Inorg Chem 6:27
49. Siegbahn PEM (1999) Inorg Chem 38:2880
50. Siegbahn PEM, Crabtree RH (1997) J Am Chem Soc 199:3103
51. Yoshizawa K, Hoffmann R (1996) Inorg Chem 35:2409
52. Yoshizawa K, Yokomichi Y, Shiota Y, Ohta T, Yamabe T (1997) Chem Lett 587
53. Yoshizawa K, Ohta T, Yamabe T, Hoffmann R (1997) J Am Chem Soc 119:12311
54. Lovell T, Li J, Noodleman L (2001) Inorg Chem 40:5267
55. Lovell T, Li J, Noodleman L (2001) Inorg Chem 40:5267
56. Mahapatra S, Halfen JA, Wilkinson EC, Pan G, Wang X, Young VG Jr, Cramer CJ, Que L Jr, Tolman WB (1996) J Am Chem Soc 118:11555
57. Bérces A (1997) Inorg Chem 36:4831
58. Lind R, Siegbahn PEM, Crabtree RH (1999) J Phys Chem B 103:1193
59. Himo F, Siegbahn PEM (2000) J Phys Chem B 104:7502
60. Siegbahn PEM, Eriksson L, Himo F, Pavlov M (1998) J Phys Chem B 102:10622
61. Siegbahn PEM (2000) Inorg Chem 39:2923
62. Siegbahn PEM, Crabtree RH (1999) J Am Chem Soc 121:117

63. Blomberg MRA, Siegbahn PEM, Styring S, Babcock G, Åkermark B, Korall P (1997) J Am Chem Soc 119:8285
64. Noodleman L, Case DA (1992) Adv Inorg Chem 38:423
65. Noodleman L (1981) J Chem Phys 74:5737
66. Parr RG, Yang W (1989) Density-functional theory of atoms and molecules. Oxford Univeristy Press, Oxford
67. Becke AD (1988) Phys Rev A 38:3098
68. Becke AD (1993) J Chem Phys 98:1372
69. Becke AD (1993) J Chem Phys 98:5648
70. Perdew JP (1992) Phys Rev B 45:13244
71. Gaussian 98 (Rev. A.6), Gaussian 03, Revision D.02, Frisch MJ, Trucks GW, Schlegel HB, Scuseria GE, Robb MA, Cheeseman JR, Montgomery Jr J A, Vreven T, Kudin KN, Burant JC, Millam JM, Iyengar SS, Tomasi J, Barone V, Mennucci B, Cossi M, Scalmani G, Rega N, Petersson GA, Nakatsuji H, Hada M, Ehara M, Toyota K, Fukuda R, Hasegawa J, Ishida M, Nakajima T, Honda Y, Kitao O, Nakai H, Klene M, Li X, Knox JE, Hratchian HP, Cross JB, Bakken V, Adamo C, Jaramillo J, Gomperts R, Stratmann RE, Yazyev O, Austin AJ, Cammi R, Pomelli C, Ochterski JW, Ayala PY, Morokuma K, Voth GA, Salvador P, Dannenberg JJ, Zakrzewski VG, Dapprich S, Daniels AD, Strain MC, Farkas O, Malick DK, Rabuck AD, Raghavachari K, Foresman JB, Ortiz JV, Cui Q, Baboul AG, Clifford S, Cioslowski J, Stefanov BB, Liu G, Liashenko A, Piskorz P, Komaromi I, Martin RL, Fox DJ, Keith T, Al-Laham MA, Peng CY, Nanayakkara A, Challacombe M, Gill PMW, Johnson B, Chen W, Wong MW, Gonzalez C, Pople JA (2004) Gaussian, Inc., Wallingford
72. Dunning TH Jr, Hay PJ (1976) Modern theoretical chemistry. Plenum, New York, pp 1–28
73. Hay PJ, Wadt WR (1985) J Chem Phys 82:270
74. Hay PJ, Wadt WR (1985) J Chem Phys 82:284
75. Hay PJ, Wadt WR (1985) J Chem Phys 82:299
76. Couty M, Hall MB (1996) J Comput Chem 17:1359
77. Baldwin MJ, Stemmler TL, Riggs-Gelasco PJ, Kirk ML, Penner-Hahn JE, Pecoraro VL (1994) J Am Chem Soc 116:11349–11356
78. Rosenzweig AC, Frederick CA, Lippard SJ, Nordlund P (1993) Nature 366:537–543
79. Rosenzweig AC, Frederick A, Lippard SJ (1996) In: Lidstrom ME, Tabita R (eds) Microbial growth on C1 compounds. Kluwer Academic Publishers, oston, pp 141–149
80. Petersson GA, Bennett A, Tensfeldt TG, Al-Laham MA, Shirley WA, Mantzars J (1988) J Chem Phys 89:2193
81. Ditchefield R, Hehre WJ, Pople JA (1971) J Chem Phys 54:724